Article

Performance Optimization of Underwater Crushing Unit Based on AHP

Lijun Wang [1],*, Shitong Jiang [1], Dongzhi Ping [1], Weilong Feng [1], Liyang Shang [2], Baoqiang Tian [1] and **Donglai Xu [3],***

[1] School of Mechanical Engineering, North China University of Water Resources and Electric Power, Zhengzhou 450045, China; x201910412319@stu.ncwu.edu.cn (S.J.); 201721704@stu.ncwu.edu.cn (D.P.); 202011905@stu.ncwu.edu.cn (W.F.); tbq123@mail.ustc.edu.cn (B.T.)

[2] Yellow River Machinery Co., Ltd., Yellow River Conservancy Commission, Zhengzhou 450006, China; 13598888532@139.com

[3] School of Computing, Engineering and Digital Technologies, Teesside University, Middlesbrough TS1 3BX, UK

* Correspondence: wanglijun@ncwu.edu.cn (L.W.); d.xu@tees.ac.uk (D.X.)

Abstract: An underwater crushing unit loaded on the underwater cleaning robot was intended to handle marine biofouling that adhered to the surface of the ship and the dam, and a prototype was initially built. A Computational Fluid Dynamics–Discrete Element Model (CFD-DEM) was created to boost the prototype's crushing performance, and its rationale was validated by contrasting the simulation results with the results of experimental tests. Accordingly, the primary influences on crushing performance and the laws governing their influence were investigated. The Analytical Hierarchy Process (AHP) method was then used to establish a prediction model for the comprehensive evaluation indicator of crushing performance. The AHP was used, in this case, because of its ability to generate the weight of indicators. The prediction model was a quadratic polynomial function with the rotational speed, the normal velocity component at the outlet of the propeller, the mass flow rate of the particles at the inlet of the unit, and the thickness of the bushing as independent variables. The prediction model fitting effect met the requirements after the test. The primary elements influencing the underwater crushing unit's performance were optimized using the prediction model. The average accumulation speed of particles in the crushing unit was reduced by 59.05%, and the mass flow rate of particles at the outlet was reduced by 11.93%. The maximum wear height of the bushing was reduced by 33.36%. The specific power was up 20.88%, and the overall crushing performance was up 9.87% when compared to before optimization.

Keywords: biofouling; CFD-DEM; AHP; regressive analysis

1. Introduction

Long-term adhesion of marine biofouling on the hull surface will greatly increase the frictional and viscous resistance of the ship in navigation and have obvious negative effects on the performance of the propeller [1], slowing down the speed of the ship by about 10% and increasing fuel consumption by up to 20% [2]. Statistics show that the US Navy spends between 180 million dollars and 260 million dollars every year to address the issue of biofouling on ship hulls [3]. The cost of the failure to shipowners is estimated to be between 500 million dollars and 1 billion dollars per year, and there is a huge market demand [4].

The hull of a ship that has excessive marine biofouling on its surface may significantly slow down the voyage, raise the cost of navigation, and reduce the ship's life span. The importance of managing and controlling hull and propeller fouling is thus emphasized by the International Maritime Organization (IMO), and maintenance schedule optimization has emerged as a significant energy-saving tool [5]. Dinariyana et al. [6] proposed the

Model-Driven Decision Support System (MD-DSS) to forecast the optimum period for underwater hull cleaning for biofouling control in order to balance the trade-off between performing maintenance and performance degradation. Degiuli et al. [7] suggest a unique methodology for scheduling a time for underwater hull cleaning. At various cleaning costs, the optimum time for underwater hull cleaning was identified.

The International Maritime Organization developed the Marpol Annex V (Prevention of Pollution by Garbage from Ships); the residue from hull scrubbing has already been defined as ship garbage, and thus the area of ship cleaning and the way of cleaning operations is restricted. Divers scrubbing ships are currently prohibited in many European ports [8]. Therefore, more energy-saving and environmentally friendly cleaning technologies should be combined with underwater robots to develop hull cleaning robots. There are many types of underwater robots, which can be functionally classified as observation-class, work-class, and special-use vehicles. A proposed observation class ROV design for the visual investigation of undersea structures was made in 2010 [9]. The system was developed to inspect pipelines, oil-producing facilities, and other infrastructure in deep waters for the Federal Mexican Oil Company. The surface unit, launching unit, tether management unit, and vehicle made up the proposed system. The vehicle includes six thrusters, a 5-function hydraulic manipulator, a 3-phase power supply for 440VAC, and was built to operate to a depth of 2000 m. A joystick was used on the surface unit to control the manipulator. To aid with a study on Lake Biwa, the largest lake in Japan, Sakagami et al. [10] created a human-sized ROV with a dual-manipulator system. To perform diverse underwater tasks, the designed ROV was outfitted with two 5-DOF manipulators. The ROV's attitude control system is equipped to maintain the vehicle's horizontal orientation and adjust its attitude in response to a variety of external factors. One operator can control the ROV's dual manipulator system and attitude control system using a newly built master-slave controller.

Underwater cleaning robots belong to the work-class of underwater robots, which are generally composed of an adsorption mechanism, moving mechanism, drive control mechanism, and cleaning operation mechanism, which realize the three functions of adsorption, moving, and cleaning, respectively [11]. To considerably lower labor intensity and increase cleaning effectiveness, a number of practical cleaning instruments have recently been produced and fitted to underwater cleaning robots. Hua et al. [12] developed a new hydroblasting cleanup system that can be loaded onto underwater cleaning robots and can effectively interrupt the growth of marine biofouling. Ralys et al. [13] designed a cavitation-generating head with a water removal system and built the prototype, avoiding the possibility that water left on the cleaned surface would decrease the effectiveness of the cavitation jet. It was preliminarily demonstrated that the method of ultrasonic-enhanced submerged cavitation jets for cleaning marine biofouling is practical by Zhong et al. [14] when they suggested a new ultrasonic-enhanced submerged cavitation jet ship fouling cleaning technique. To remove adhered barnacle fouling, Tian et al. [15] suggested a step-by-step CO_2/nanosecond hybrid laser cleaning procedure. The upper parietal shell and the main body are completely peeled off in the first step because the CO_2 laser heats the exterior shell. The bottom remaining base plate, cement layer, and biofilm are removed in the second step using a nanosecond laser. In addition, underwater cleaning robots need sufficient adhesion to maintain continuous and reliable contact with hulls with different types of contact characteristics. Technologies that provide adhesion include three categories, namely magnetic adsorption, vacuum adsorption, and thrust adsorption. Fan et al. [16] proposed an underwater climbing robot with a combined magnet adhesion unit for the removal of continuous areas on the surface of submerged pipes on marine platforms. Robots for cleaning the hull of ships were given a flexible wheel-leg composite moving mechanism by Wang et al. [17]. The three leg frames that make up the designed changeable wheel leg on the rotating shaft increase the movement space by removing the magnetic wheel's positional restrictions. The robot has good motion stability, according to the simulation data. Chen et al. [18] developed a robotic solution in which the robot is driven by propellers and tracks to climb up the hull and remove dirt from the hull using a cavitation water jet

method. In addition, the robot can adhere to the hull surface and can climb the hull stably. Hachicha et al. [19] developed a hull underwater cleaning robot called ARMROV, which uses propellers to attach to the hull and is equipped with two-manipulator arms, each with a water gun at the end, using high-pressure water for removal. For the autonomous cleaning of hull niche areas, Park et al. [20] suggested an autonomous cleaning robot system based on a hydraulic robot arm with several degrees of freedom. The robot generates the relative coordinates of the ROI within the niche region used for cleaning by estimating the propeller position and positioning data as a typical niche area of the hull using an underwater laser scanner. Although these underwater cleaning robots have better cleaning ability and adsorption performance, they do not have a recycling function.

An underwater tracked vehicle with a rock crushing (RC) tool was developed by Vu et al. [21]. An RC tool is a device used in mining and civil engineering that excavates rock using a rotary cutting unit outfitted with cutter tools (bits). Using design synthesis principles, a subaquatic crusher was created that can reduce mined nodules from a maximum size of 100 mm to a crushed size of 30 mm [22]. These underwater crushing devices lack a self-contained collection system.

Marine biofouling cleaned from the hull is often left in the dock, and the removal of marine biofouling requires staff to filter and salvage it, which is time-consuming and labor-intensive; if not cleaned in time, it will cause pollution to the water body. Some of the underwater cleaning robots have a recycling function, but when the marine biofouling passes through the conveying pipeline, the conveying pipeline is easily blocked by particles of large size, thus affecting the efficiency of the underwater cleaning robot.

In order to solve the above problems, an underwater crushing unit with a crushing function applied to underwater cleaning robots is proposed in this paper, and a prototype of this underwater crushing unit is fabricated. Based on the geometric model of the underwater crushing unit, a simulation model of the underwater crushing device based on CFD-DEM is established. A comprehensive performance optimization method based on multiple nonlinear regression and AHP is proposed.

The novelty of this paper is as follows: to the best of the authors' knowledge, the proposed device is the first underwater crushing device with crushing and recovery functions for underwater cleaning robots. The novelty of the performance optimization method used in this paper is the application of a multi-attribute decision method to the comprehensive performance optimization of the mechanism, which is able to balance the values of these evaluation indicators to be optimized based on the weights of multiple evaluation indicators.

This paper is organized as follows: in Section 2, the structure of the underwater crushing unit and the building method of the simulation model are introduced. Section 3 discusses the factors influencing crushing performance and develops prediction models for each evaluation indicator. In Section 4, the prediction model of the comprehensive evaluation indicator is established by combining the AHP, and the model is solved to obtain the optimal combination of factors. Finally, Section 5 discusses the optimization results, limitations of the study, and prospects for future research.

2. CFD-DEM Modeling, Simulation, and Validation

2.1. Infrastructure and Methods

After preliminary design, the initial structure of the underwater crushing device was determined. The 3D structure of the underwater crushing unit is schematically shown in Figure 1.

To be able to employ the underwater cleaning robot to remove the marine biofouling from the ship's surface, the underwater crushing unit must be installed as a necessary component. An external connection provides electricity to the underwater cleaning robot. The propeller and motor are connected to a power supply cable, which is an umbilical cable, to supply the electricity required for rotation. The underwater cleaning robot also contains

a controller that allows for remote control of its operation. The propeller and motor are connected to this controller and are started and stopped by it.
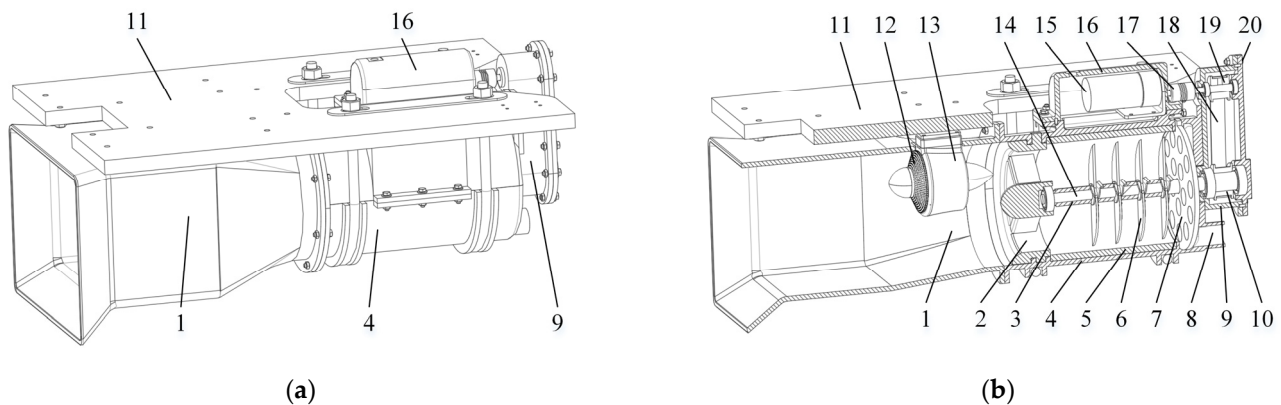

(**a**)   (**b**)

Figure 1. Schematic diagram of the structure of the underwater crushing unit. (**a**) Schematic diagram of the overall structure of the underwater crushing unit; (**b**) Schematic diagram of the cross-sectional structure of the underwater crushing unit. In the Figure, 1—Collection bin; 2—Support ring; 3—Limit tube; 4—Crushing bin; 5—Bushing; 6—Blade; 7—Filter plate; 8—Drain port; 9—Waterproof case for the belt; 10—Upper pulley; 11—Part of the framework; 12—Filter cover for the propeller; 13—Propeller; 14—D-Shaft; 15—Motor; 16—Waterproof cover for the motor; 17—Coupling; 18—Belt; 19—Lower pulley; 20—Waterproof cover for belt.

A solid-liquid pump is installed at one end of the conveying pipeline, and a conveying pipeline is installed at the drain port after the underwater crushing machine and underwater cleaning robot have been installed as a single unit. While the propeller, motor, and solid-liquid pump of this underwater crushing unit are commanded to start, the underwater cleaning robot is submerged in the water, and the hull surface is cleaned by human control of the underwater cleaning robot.

The propeller with the same flow speed of inlet and outlet is selected, and after the propeller is started, according to Bernoulli's equation [23]:

$$z + \frac{p}{\rho g} + \frac{v^2}{2g} = C \tag{1}$$

where z is the potential energy per unit of gravity fluid, $p/\rho g$ is the pressure energy per unit of gravity fluid, $v^2/2g$ is the kinetic energy per unit of gravity fluid, and C is the constant of integration. The greater the flow velocity v somewhere in the fluid, the smaller the pressure p. Thus, there are low-pressure areas on the left and right sides of the propeller, which is located in the collection bin. Marine biofouling on the hull is collected with the water flow to the low-pressure area in the collection bin. Marine biofouling reaches both ends of the propeller and enters the crushing bin under the action of the thrust generated by the blade of the propeller. Once the motor is running, its output shaft causes the upper pulley to spin through the connection, the upper pulley causes the lower pulley to do rotary motion, the lower pulley causes the blade to move, and the blade smashes the biofouling that enters the crushing bin.

Marine biofouling in the crushing bin goes to the drain port once the solid-liquid pump starts to produce suction in the crushing bin at the drain port. The user filters and recycles the crushed biofouling after marine biofouling is discharged to the shore via a drain port, conveying pipeline, and solid-liquid pump.

The prototype was built based on the 3D model of the underwater crushing unit, as shown in Figure 2, with a rotational speed of the blade of 700 r/min, a normal velocity component of 1.5 m/s at the outlet of the propeller, and a bushing thickness of 4.6 mm. The barnacle shells inside the underwater crushing unit accumulated too fast, which required the underwater cleaning robot to stop and stay in place to crush the barnacle shells inside

the device, which affected the overall cleaning efficiency of the underwater cleaning robot. Therefore, the overall performance of the underwater crushing unit needs to be optimized.
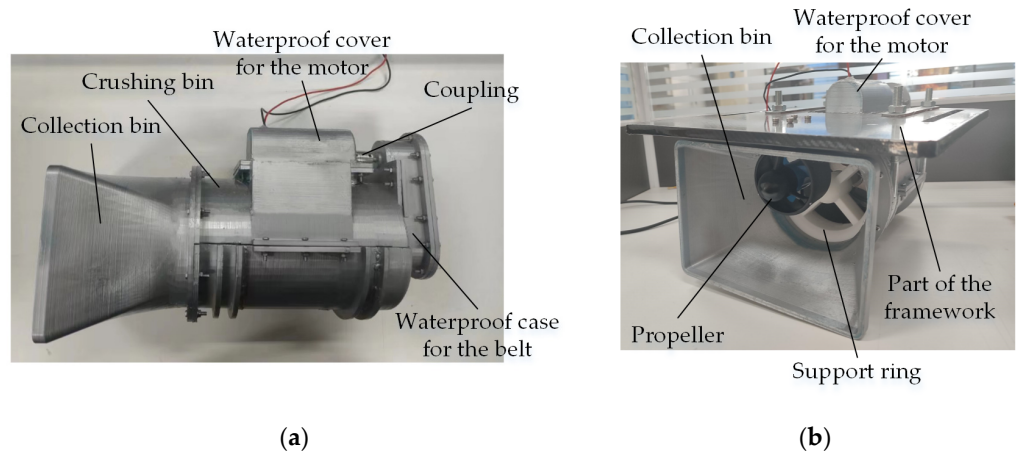

Figure 2. Prototype. (**a**) Side view of the prototype; (**b**) Isometric view of the prototype.

2.2. Structural Simplification and CFD-DEM Modeling

Performance optimization required a simulation model of the prototype underwater crushing unit. In the actual working conditions of the underwater crushing unit, its interior was full of seawater and marine biofouling. Therefore, CAE pre-processing software was used to extract the fluid domain of the underwater crushing unit. Then, the fluid domain model was imported into the DEM software and CFD software to establish the discrete element simulation model and the fluid simulation model, respectively. Finally, the CFD-DEM coupling model was established through the coupling interface file.

2.2.1. Model Parameter Setting in RockyDEM

The Boundary Collision Statistics model was enabled, and the Intensities collection was set to active. Models of the fluid domain, rotating blade, liner, and filter plate were imported into RockyDEM, and the wear model of the liner was enabled. According to the actual operation of the prototype, the rotational speed of the blade and the mass flow rate at the inlet were set to 700 m/s and 180 g/s, respectively, and both parameters were enabled at 2 s. The total simulation time was set to 10 s, and the crushing start time was set to 2 s. Among the marine biofouling materials, mainly barnacles and mussels, the mineralized tissue in the barnacle shell plate was mainly composed of calcite, which is also the main component of limestone and marble [24], and barnacles are closer to limestone in nature. Because of the composition and variety of marine biofouling, limestone particles with properties and shapes close to those of barnacle shells were used as simulation particles to simplify the simulation, as shown in Figure 3.
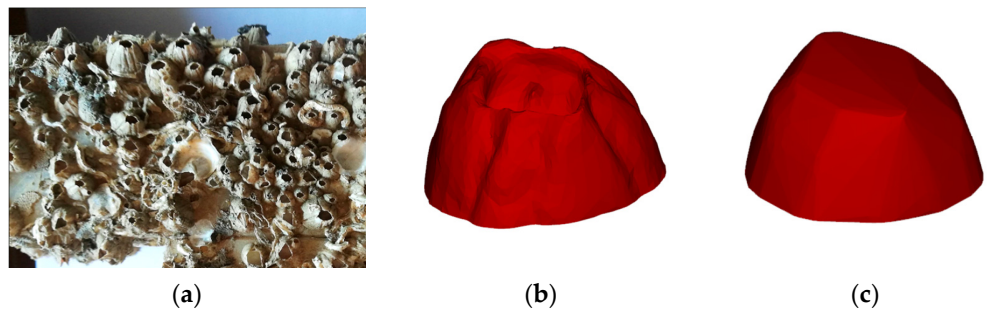

Figure 3. Barnacle shells and the simulation particle. (**a**) Barnacle shells [25]; (**b**) Simulation particle before being smoothed; (**c**) Simulation particle before being smoothed.

The material properties of limestone particles and steel and their collision parameters are shown in Table 1.

Table 1. Material properties of limestone particles and steel and their collision parameters [26].

Parameters	Value	Unit
Density of limestone	2650	kg/m^3
Young's modulus of limestone	5.23×10^8	Pa
Poisson's ratio of limestone	0.25	-
The density of steel (304)	7930	kg/m^3
Young's modulus of steel (304)	2.04×10^{11}	Pa
Poisson's ratio of steel (304)	0.285	-
Coefficient of limestone-limestone static friction	0.77	-
Coefficient of limestone-limestone rolling friction	0.1	-
Coefficient of limestone-limestone restitution	0.208	-
Coefficient of limestone-steel static friction	0.61	-
Coefficient of limestone-steel rolling friction	0.07	-
Coefficient of limestone-steel restitution	0.557	

The Ab-T10 model was chosen as the breakage model for the particles. This model worked with any non-round solid particle shape that comes with Rocky. To calculate $A \cdot b$, the following units and expression were used:

$$A \cdot b = 3600 \cdot M \cdot S \tag{2}$$

where M is the maximum t_{10} value (%), which can be determined by the drop weight test; S is the selection function coefficient, which is a measure of the material hardness. The Ab-T10 model parameters are shown in Table 2 [27]. The Fluent Two Way was selected to establish the CFD-DEM coupling model.

Table 2. Particles t_{10} parameters.

Parameters	Value
A	54.5
b	0.018
$A \cdot b$	0.98
t_{10}	10%

2.2.2. Pre-Processing and Parameter Settings in Fluent

The application scenario of the underwater crushing unit is usually shipyards, wharves, and dams, and the internal flow medium of the underwater crushing unit is liquid seawater. Therefore, the crushing device flow medium was simulated as an incompressible fluid.

To simplify the calculation, the propeller was simplified as a rotary body with the same flow speed and opposite flow direction at both ends. The geometry of the crushing unit was simplified in Solidworks, the simplified model was imported into Spaceclaim, and the fluid domain of the crushing unit was extracted using the volume extract function. The fluid domain model was meshed in Ansys, and the Inlet_1, Inlet_2, Inlet_3, Outlet, and Wall were defined and imported into Fluent, as shown in Figure 4. The correlation between the residual mass of particles in the underwater crushing unit and the number of grids was tested, and the results are shown in Figure 5. The number of grids was determined as 300,588. Figure 4c shows the dimensional parameters of the fluid domain, and the values of the geometric parameters are shown in Table 3.

(a)
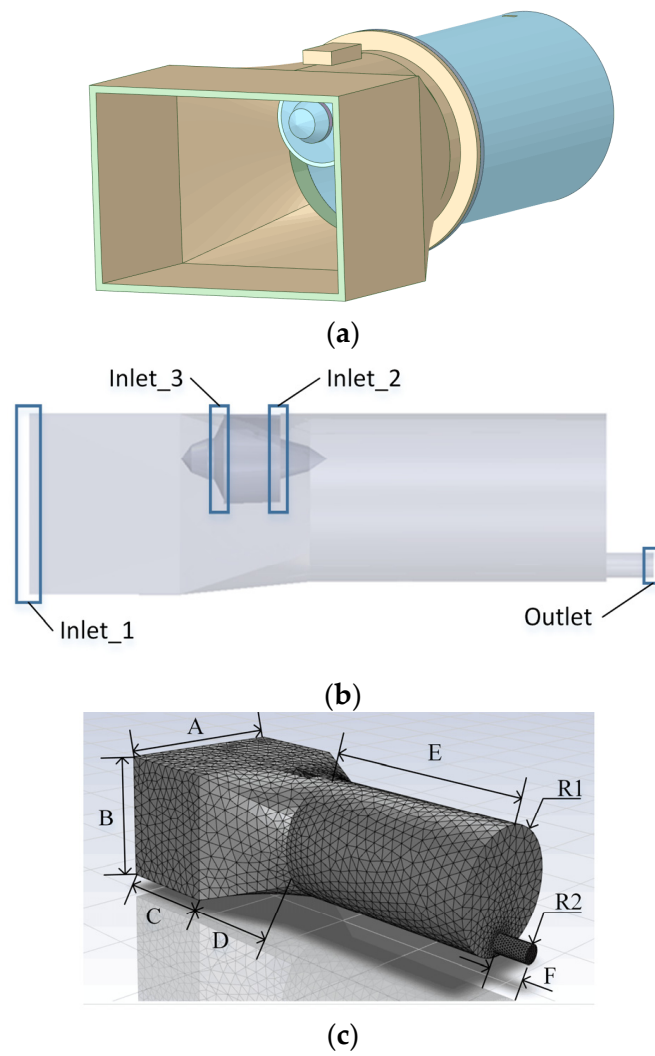

(b)

(c)

Figure 4. Fluid domain model pre-processing. (**a**) Simplified geometry of the underwater crushing unit; (**b**) Geometry of the fluid domain; (**c**) Geometry of the meshed fluid domain.
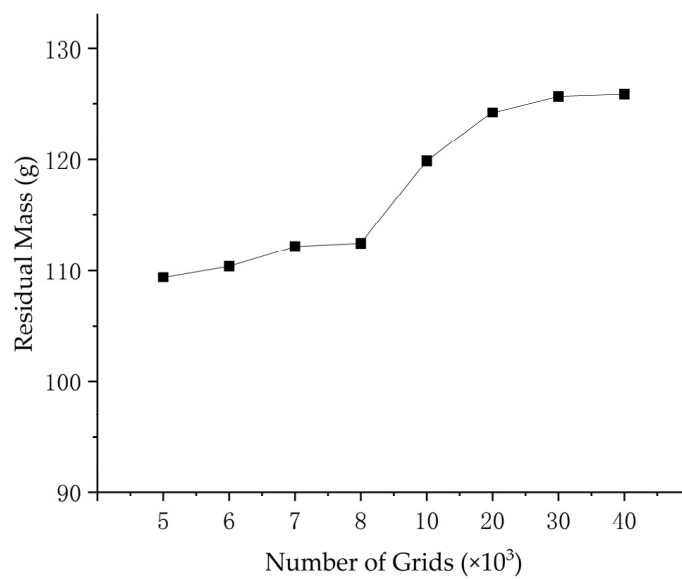

Figure 5. Grid convergence test.

Table 3. Value of the dimensional parameters of the fluid domain.

Parameters	Value (mm)
A	200
B	140
C	115
D	100
E	225
F	36
R1	65
R2	10

The parameters in the table correspond to Figure 4c.

Steady flow in a channel or pipe depends only on the Reynolds number. The equation for the Reynolds number is [23]:

$$R_e = \frac{\rho v D}{\mu} \tag{3}$$

where ρ is the density, v is the flow velocity, D is the hydraulic diameter, and μ is the dynamic viscosity.

For non-circular pipes, the hydraulic diameter was calculated with the generic equation:

$$D_H = \frac{2ab}{a+b} \tag{4}$$

where a and b are the length and width of the rectangular pipe section, respectively. After calculation, $D_H = 0.1647$ mm. The test simulation working medium is liquid seawater under standard conditions, with density $\rho = 1.030 \times 10^3$ kg/m^3 and dynamic viscosity $\mu = 1.61 \times 10^{-3}$ Pa·s. The underwater cleaning robot traveled at a minimum velocity of 0.5 m/s on the hull surface, so the inlet flow velocity of the underwater crushing unit was taken as $v = 0.5$ m/s. Substituting the above parameters into Equation (3), it can be seen that the Reynolds number $R_e = 52,683.54 > 4000$ at the inlet of the underwater crushing unit. In this case, the flow state at the inlet of the unit was fully turbulent. Therefore, the simulation needed to use the turbulence model. The standard K-epsilon model and Scalable Wall Functions were used for the turbulence model. The boundary conditions are shown in Table 4, and the residuals of convergence for each variable were 10^{-3}.

Table 4. Boundary conditions.

	Boundary Conditions
Inlet_1	Velocity inlet with of 0.5 m/s
Inlet_2	Velocity inlet with of 1.5 m/s
Inlet_3	Velocity inlet with of −1.5 m/s
Outlet	Pressure outlet

The number of time steps and time step size were set to 1000 and 0.001 s, respectively, and the calculated Yplus values at each part of the wall are shown in Figure 6.
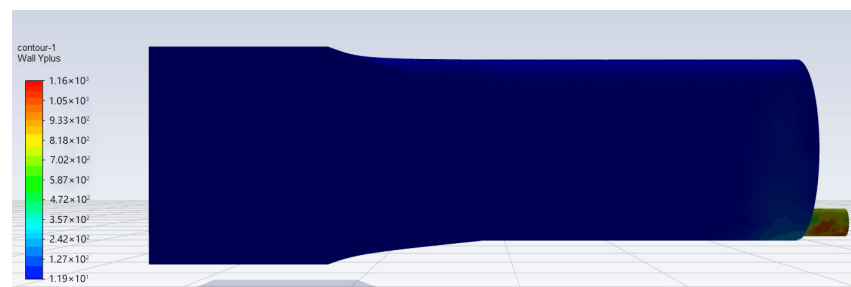

Figure 6. Contours of wall Yplus.

After starting the simulation, the blade and particle inlet were not activated for the first 2 s to obtain the fluid domain model filled with fluid, and from 2 s onwards, the breakage model was active. The particles are given different colors depending on the particle size range, as shown in Figure 7.
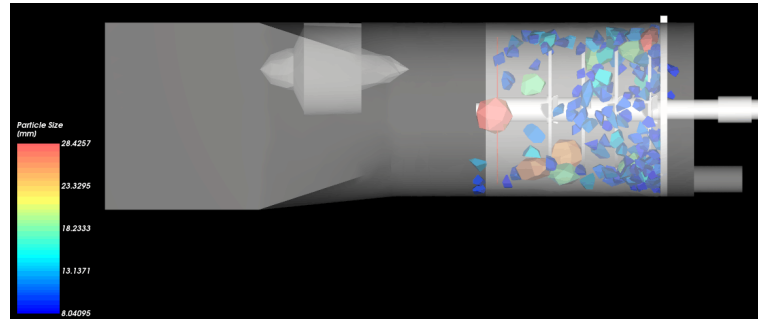

Figure 7. Simulation interface of the underwater crushing unit in RockyDEM.

2.3. Validation of the CFD-DEM Model

In order to validate the CFD-DEM, the underwater crushing unit was tested in an underwater environment. Figure 8 shows the experimental setup.

(**a**)

(**b**)
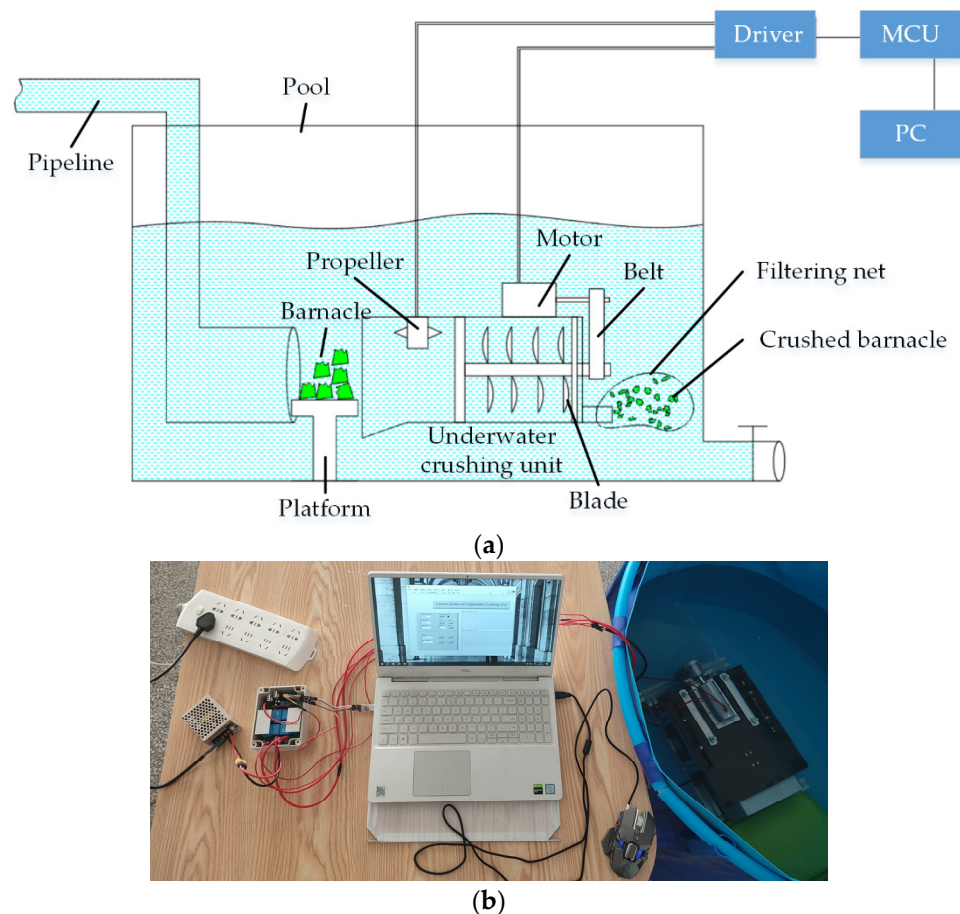
Figure 8. Experimental setup. (**a**) Schematic of the experimental setup; (**b**) Top view of the experimental setup.

Labview is used as the upper computer software for the controller of the underwater crushing unit, which communicates with the microcontroller through the serial port. The microcontroller controls the motor driver to regulate the rotational speed of the and the flow velocity of the propeller. The underwater crushing device was placed into a pool with

a diameter of 1 m and a depth of 0.8 m. The barnacle shell was placed on a platform at the entrance to the unit. In order to collect crushed barnacles, a nylon filter mesh with 20 mesh was installed at the drain port. A water pipeline with a flow velocity of 0.5 m/s was installed at the entrance of the underwater crushing unit.

The surface of the barnacle shell was rinsed and dried and used as a test sample, as shown in Figure 9a. Then, 150 g of intact barnacle shells were weighed and placed on the entrance platform. The flow velocity of the propeller was adjusted to 1.5 m/s, and the rotational speeds were adjusted to 500 r/min, 700 r/min, 900 r/min, 1100 r/min, and 1300 r/min. The tests were conducted under five different working conditions with a duration of 5 s.

(**a**)
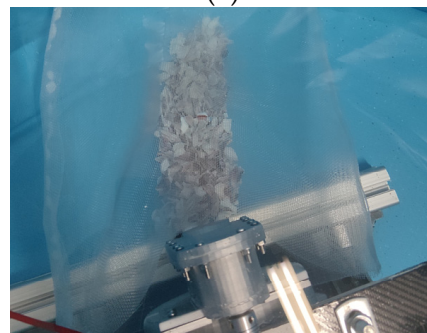
(**b**)

Figure 9. Barnacle shell. (**a**) The rinsed and dried barnacle shell; (**b**) The crushed barnacle shell.

The crushed barnacle shell (Figure 9b) collected by the filter were weighed. Then, the five working conditions mentioned above were simulated for 5 s using the CFD-DEM, and the simulation results were compared with the results of the experimental tests, as shown in Figure 10.

As can be seen from Figure 10, with the increase in the rotational speed of the underwater crushing unit, the mass of the crushed barnacle shells flowed out at the same time gradually increased and approached 190 g. Generally speaking, the change rule between the simulation value and the experimental value was consistent. When the rotational speed was lower, the test value was slightly larger than the simulation value, and when the rotational speed was higher, the test value was slightly smaller than the simulation value. The reason for this is that the higher the rotational speed, the greater the displacement of part of the barnacle shell toward the entrance when it collides with the blades. These reverse-displaced barnacle shells will again move toward the drain port under the influence of the water flow. The error decreased as the rotational speed increased and stabilized below 10%. The errors were due to the simplified structure of the simulation model, non-zero tangential flow velocity at the outlet of the propeller, vibration of the test rig as a whole, and insufficient stiffness of the blade shaft.
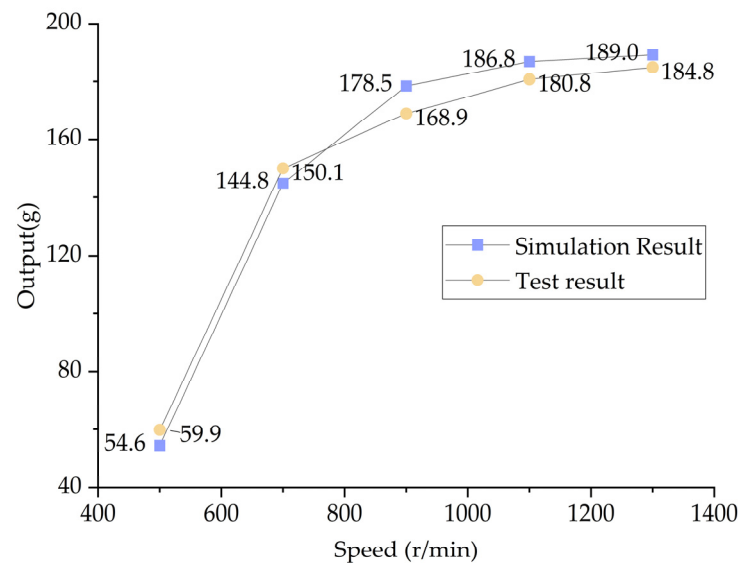
Figure 10. Results of CFD-DEM simulation and experimental test.

3. The Impact of Various Factors on Crushing Performance

3.1. Simulation Scheme Selection Based on Uniform Design

After comparing each U-table, the factor-level table is listed in combination with linear interpolation, and factor-level table is shown in where t is the total simulation time, m_{re} is the remaining mass of the particles at the end of the simulation, and t_b is the time from the beginning of the simulation to the first broken particle outflow. Parameters t, m_{re}, and t_b were obtained in RockyDEM.

In the Table 5, x_1 is the rotational speed of the blade, x_2 is the normal velocity component at the outlet of the propeller, x_3 is the mass flow rate of the particles at the inlet, x_4 is the thickness of the bushing; y_1 is the maximum wear height of the bushing, y_2 is the mass flow rate of the particles at the outlet, y_3 is the average accumulation speed of the particles in the underwater crushing unit, y_4 is the specific power (i.e., the power consumed per unit mass of particles crushed).

Table 5. Factor-level table.

No.	x_1 (r/min)	x_2 (m/s)	x_3 (g/s)	x_4 (mm)	y_1 (mm)	y_2 (g/s)	y_3 (g/s)	y_4 (W/g)
1	200	0.6	145	4.6	1.52	82.97	62.03	0.109
2	275	1.05	195	5.6	2.07	120.53	74.47	0.141
3	350	1.5	245	6.6	2.62	158.09	86.91	0.172
4	500	2.4	70	4.2	1.58	63.03	6.97	0.253
5	575	1.2	120	5.2	2.16	104.73	15.27	0.270
6	650	0	170	6.2	2.75	146.44	23.56	0.287
7	800	0.9	270	3.8	2.70	201.68	68.32	0.397
8	875	1.35	182.5	4.8	2.39	144.86	37.64	0.520
9	950	1.8	95	5.8	2.09	88.04	6.96	0.643
10	1100	2.7	195	3.4	2.51	163.58	31.42	0.481
11	1175	1.5	245.	4.4	2.78	213.5	31.5	0.562
12	1250	0.3	295	5.4	3.06	263.43	31.57	0.642
13	1400	1.2	120	3.0	1.41	30.49	89.51	0.453
14	1475	1.65	170	4.0	1.91	117.7	52.3	0.474
15	1550	2.1	220	5.0	2.41	204.92	15.08	0.495
Before optimization	700	1.5	180	4.6	2.32	150.68	29.31	0.311

The mass flow rate of particles at the outlet y_2 and the average accumulation speed y_3 of particles were calculated by Equations (4) and (5), respectively:

$$y_2 = \frac{x_3 t - m_{re}}{t - t_b} \tag{5}$$

$$y_3 = \frac{m_{re} - x_3 t_b}{t - t_b} \tag{6}$$

where t is the total simulation time, m_{re} is the remaining mass of the particles at the end of the simulation, and t_b is the time from the beginning of the simulation to the first broken particle outflow. Parameters t, m_{re} and t_b can be obtained in RockyDEM.

3.2. The Best-Influencing Factor Corresponding to the Evaluation Index of Crushing Performance

The quadratic polynomial regression equation model was as follows:

$$y_k = a + \sum_{i=1}^{4} b_i x_i + \sum_{i=1}^{4} c_i x_i^2 + \sum_{i=1}^{3} \sum_{j=i+1}^{4} d_{ij} x_i x_j, (k = 1, 2, 3, 4) \tag{7}$$

where a, b_i, c_i, d_{ij} are constants. Based on the Table 5 data, a quadratic polynomial stepwise regression analysis was performed, and the maximum wear height of the bushing, the mass flow rate of particles at the outlet, the average accumulation speed of particles in the crushing unit, and the specific power prediction models were obtained after removing the insignificant polynomials:

$$y_1 = -2.940 - 1.286x_2 + 0.012x_3 + 1.244x_4 + 0.426x_2^2 - 0.218x_4^2 + 0.008x_2x_3 + 0.051x_2x_4 \tag{8}$$

$$\begin{aligned} y_2 = & -1467.919 + 0.951x_1 - 844.703x_2 + 1.575x_3 + 624.206x_2 + 161.254x_2^2 - 56.602x_4^2 - 0.213x_1x_2 - 0.133x_1x_4 \\ & + 0.912x_2x_3 + 91.295x_2x_4 - 0.441x_3x_4 \end{aligned} \tag{9}$$

$$\begin{aligned} y_3 = & 455.029 - 0.171x_1 + 220.916x_2 + 0.033x_3 - 195.554x_4 - 51.915x_2^2 + 18.419x_4^2 \\ & + 0.107x_1x_2 - 0.51x_2x_3 - 18.882x_2x_4 + 0.171x_3x_4 \end{aligned} \tag{10}$$

$$y_4 = 8.59 - 0.01x_1 + 5.31x_2 - 3.78x_4 - 0.90x_2^2 + 0.35x_4^2 - 0.60x_2x_4 \tag{11}$$

The analysis of variance (ANOVA) table for the prediction models is shown in Table 6.

Table 6. The ANOVA table for the regression equations.

Equations	Source	SS	df	MS	F	R^2
y_1	Regression	80.380	4	20.095	18,826.706	0.997
	Residual	0.011	10	0.001		
y_2	Regression	350,659.796	4	87,664.949	17,044.492	0.999
	Residual	51.433	10	5.143		
y_3	Regression	37,702.612	4	9425.653	572.059	0.985
	Residual	164.767	10	16.477		
y_4	Regression	2.725	4	0.681	219.380	0.929
	Residual	0.031	10	0.003		

By consulting the F Distribution Table, the Table of Critical Values for Coefficients of Correlation, and Table 6, it can be seen that: $F > F_{0.01}(4, 10) = 5.99$, $R_{min} = 0.840$, $R^2 > R_{min}^2 = 0.7056$ for each regression equation. Therefore, the four regression equations established were very significant and fit well with the experimental data, and the prediction model was highly representative.

The planning solution of Equations (8)–(11) showed that, theoretically, when the rotational speed of the blade was 772 r/min, the normal velocity component at the propeller

outlet was 0.04 m/s, the mass flow rate at the inlet was 77.07 g/s, and the thickness of the bushing was 3.27 mm, and the minimum bushing wear height was 2.27 mm. When the rotational speed of the blade was 268.28 r/min, the normal velocity component at the outlet of the propeller was 0.18 m/s, the mass flow rate at the inlet was 270 g/s, and the thickness of the bushing was 3.93 mm, the mass flow rate of the particles at the outlet was the maximum close to 270 g/s, and the crushing efficiency of the crushing unit was the highest at this time. When the rotational speed was 874.9 r/min, the normal velocity component at the outlet of the propeller was 1.35 m/s, the mass flow rate at the inlet was 183.17 g/s, and the thickness of the bushing was 4.82 mm, the average accumulation speed of the particles in the underwater crushing unit was the smallest and close to 0 g/s, and the accumulation speed of the particles in the crushing unit was the slowest. When the rotational speed was 1600 r/min, the normal velocity component at the outlet of the propeller was 2.17 m/s, the mass flow rate at the inlet was 70 g/s, and the thickness of the bushing was 4.11 mm. The specific power could obtain the minimum value of 0.086 W/g when the rotating shaft of the rotating blade had the longest service life.

4. Comprehensive Crushing Performance Optimization (AHP)

AHP is a comprehensive evaluation method combining qualitative analysis and quantitative calculation, which does not require a large amount of historical data and only requires decision-makers to use their own experience to judge the importance of each factor. Thus, AHP can provide a concise and practical decision-making method for some multi-objective complex problems. The best combination of influencing factors corresponding to each evaluation indicator of crushing performance is not consistent, so it is convenient to combine AHP, consider the influence of four indicators on crushing performance, establish a comprehensive evaluation prediction model of crushing performance, and obtain the optimal combination of influencing factors.

4.1. Hierarchy between Factors and Indicators

By grouping all influencing factors and indicators into layers, the structural model had three layers, as shown in Figure 11. The comprehensive evaluation indicator (i.e., crushing performance) Z was in the Target Layer. The maximum wear height of the bushing A_1, the mass flow rate of particles at the outlet A_2, the average accumulation speed of particles in the crushing unit A_3 and the specific power A_4 are four indicators in the Indicator Layer, the rotational speed B_1, the normal velocity component of the propeller outlet B_2, the mass flow rate of particles at the inlet B_3, and the thickness of the bushing B_4 are four factors in the Factor Layer.
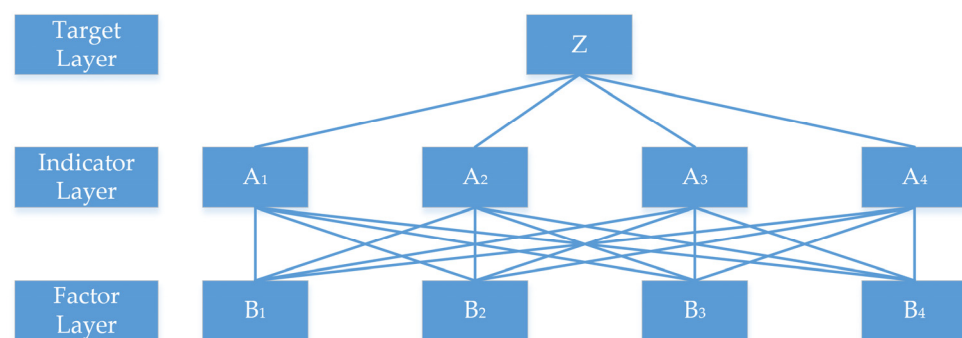

Figure 11. Hierarchy diagram.

4.2. Construct the Judgment Matrix

Based on the hierarchical model, all judgment matrices in this model were constructed by comparing the relative importance of this layer with a factor in the previous layer. In the two-factor M and N importance analysis, a scale of 1 to 9 was used to assign values, as shown in Table 7.

Table 7. Comparison of the importance of the factors.

Ratio Scale (M/N)	Meaning
1	M and N have the same importance.
3	M is slightly more important than N.
5	M is significantly more important than N.
7	M is strongly more important than N.
9	M is extremely important than N.
2, 4, 6, 8	The importance of M compared to N is between the above 2 adjacent levels.
Countdown	The comparative value of the importance of M and N is the inverse of the above value.

In the actual operation of the underwater crushing unit, the efficiency of marine biofouling being discharged from the crushing unit should be ensured first, so the mass flow rate of the particles at the outlet has a relatively large impact on the total target crushing performance. The accumulated mass of marine biofouling in the crushing unit will greatly increase the power consumption and bushing wear, and when the accumulated mass reaches a certain amount, the underwater cleaning robot needs to stop moving forward and stop collecting marine biofouling to reduce the accumulated mass of marine biofouling in the crushing unit, so the accumulated mass of particles in the crushing unit takes priority over power consumption and bushing wear. In the crushing process, power consumption accounts for a large proportion, although the economic type and crushing performance of the crushing unit will also be affected due to bushing wear. If the power consumption can be effectively reduced, more cost savings can be achieved.

The mass flow rate of the particles at the outlet can be thought of as slightly more important for the target layer in the weight calculation than the average accumulation speed of the particles in the crushing unit, which is in turn slightly more important than the specific power. The maximum wear height of the bushing was the least important among the performance indicators. According to the definition of importance, the judgment matrix constructed in the crushing performance prediction model is:

$$
Q_{AZ} = \begin{bmatrix} 1 & 1/7 & 1/5 & 1/3 \\ 7 & 1 & 2 & 2 \\ 5 & 1/2 & 1 & 2 \\ 3 & 1/2 & 1/2 & 1 \end{bmatrix} \tag{12}
$$

Similarly, in the prediction models for the maximum wear height of the bushing, the mass flow rate of the particles at the outlet, the average accumulation speed of the particles in the crushing unit, and the specific power, the judgment matrices constructed are:

$$
Q_{BA_1} = \begin{bmatrix} 1 & 1/7 & 3 & 1/5 \\ 7 & 1 & 9 & 2 \\ 1/3 & 1/9 & 1 & 1/8 \\ 5 & 1/2 & 8 & 1 \end{bmatrix} \tag{13}
$$

$$
Q_{BA_2} = \begin{bmatrix} 1 & 1/7 & 1/3 & 1/5 \\ 7 & 1 & 6 & 3 \\ 3 & 1/6 & 1 & 1/4 \\ 5 & 1/3 & 4 & 1 \end{bmatrix} \tag{14}
$$

$$
Q_{BA_3} = \begin{bmatrix} 1 & 1/9 & 1/3 & 1/7 \\ 9 & 1 & 5 & 2 \\ 3 & 1/5 & 1 & 1/4 \\ 7 & 1/2 & 4 & 1 \end{bmatrix} \tag{15}
$$

$$Q_{BA_4} = \begin{bmatrix} 1 & 1/6 & 2 & 1/7 \\ 6 & 1 & 8 & 1/2 \\ 1/2 & 1/8 & 1 & 1/9 \\ 7 & 2 & 9 & 1 \end{bmatrix} \tag{16}$$

4.3. Calculate the Weight between Adjacent Layers

Single hierarchical ranking refers to the calculation of the weights of the relative importance of factors in this hierarchy according to the judgment matrix for a factor in the upper level of the hierarchy. Using the normalized eigenvector of the judgment matrix as the weight vector, the sum-product method solves the weight vector process as follows: First, the judgment matrix is normalized by column:

$$\overline{a_{ij}} = a_{ij} / \sum_{i=1}^{n} a_{ij} \tag{17}$$

Then, the normalized matrix is summed by rows to obtain the sum vector:

$$W_i = \left(\sum_{j=1}^{n} \overline{a_{ij}} \right) \tag{18}$$

Next, the matrix is averaged to obtain the weight vector:

$$\overline{W} = W_i / \sum_{i=1}^{n} W_i \tag{19}$$

Finally, the maximum eigenvalue of the matrix λ_{max} is calculated. The weight vector is the normalized eigenvector corresponding to the maximum eigenvalue λ_{max} of the judgment matrix A.

$$\lambda_{max} = \sum_{i=1}^{n} \left[(A\overline{W}_i)_i / (n\overline{W}_i)_i \right] \tag{20}$$

where a_{ij} is the element of the judgment matrix, W_i is the sum vector of the normalized matrix, and $\overline{W}_i$ is the weight vector of the judgment matrix.

When λ_{max} is obtained, a consistency test needs to be performed to ensure the reliability of the evaluation results. The test equation is as follows:

$$CR = CI/RI \tag{21}$$

$$CI = (\lambda_{max} - n)/(n - 1) \tag{22}$$

where λ_{max} is the maximum eigenvalue of the judgment matrix, n is the order of the matrix, CI is the consistency indicator, and RI is the random consistency indicator. RI can be found in Table 8 [28].

Table 8. Random consistency indicator *RI*.

Size (n)	1	2	3	4	5	6	7	8	9
RI	0.00	0.00	0.58	0.90	1.12	1.24	1.32	1.41	1.45

If $CR < 0.1$, the degree of inconsistency of the judgment matrix is within the tolerance range, there is satisfactory consistency, the matrix can be accepted by the consistency test, and its feature vector can be used as the weight vector. Otherwise, the matrix needs to be further adjusted.

According to the sum-product method, the weight vectors of the four indicators in the Indicator Layer are obtained as $\overline{W} = (0.121, 0.417, 0.27, 0.192)$, and the maximum

eigenvalue of the judgment matrix is $\lambda_{\max} = 4.042$, $CI = 0.014$, $RI = 0.90$, $CR = 0.016 < 0.1$, which satisfies the consistency test.

The judgment matrix and consistency test parameters of the four factors in the factor layer relative to the four indicators in the Indicator Layer are shown in Table 9.

Table 9. Results of judgment matrix.

Judgment Matrix	Weight Vector	$\lambda_{\max}$	CI	CR
Q_{BA_1}	$\overline{W_1} = (0.09, 0.531, 0.043, 0.336)$	4.101	0.034	0.038
Q_{BA_2}	$\overline{W_2} = (0.056, 0.562, 0.108, 0.274)$	4.177	0.059	0.066
Q_{BA_3}	$\overline{W_3} = (0.046, 0.519, 0.108, 0.327)$	4.061	0.020	0.023
Q_{BA_4}	$\overline{W_1} = (0.075, 0.351, 0.046, 0.528)$	4.062	0.021	0.023

4.4. Calculate the Weight between the Bottom and Top Layers

The total hierarchical ranking is the process of determining the ranking weights of all factors in the Factor Layer relative to the importance of the Target Layer. As can be seen in Figure 11, the Indicator Layer has four factors A_1, A_2, A_3, and A_4, and the weights to the Target Layer Z are a_1, a_2, a_3, and a_4, respectively. The Factor Layer has four factors B_1, B_2, B_3, and B_4, and the hierarchical single ranking of the factors in the Indicator Layer are b_{1j}, b_{2j}, b_{3j}, and b_{4j}, respectively, where b_{ij} denotes the importance of b_i to a_j (i, $j = 1, 2, 3, 4$). The total hierarchical ranking of the Factor Layer is:

$$\begin{cases} B_1 : b_1 = \sum_{j=1}^{4} a_j b_{1j} \\ B_2 : b_2 = \sum_{j=1}^{4} a_j b_{2j} \\ B_3 : b_3 = \sum_{j=1}^{4} a_j b_{3j} \\ B_4 : b_4 = \sum_{j=1}^{4} a_j b_{4j} \end{cases} \tag{23}$$

For this hierarchical total ranking, it is also necessary to perform a consistency test. The test equation is as follows:

$$CR = \sum_{j=1}^{4} a_j CI_j / \sum_{j=1}^{4} a_j RI_j \tag{24}$$

where CI_j is the hierarchical single rank consistency indicator of each factor in the Factor Layer to each indicator in the Indicator Layer, RI_j is the random consistency indicator of each factor in the Factor Layer to each indicator in the Indicator Layer. Similarly, when $CR < 0.1$, it is considered that the hierarchical total ranking passes the test.

From the hierarchical total ranking test, Equation (24), it can be obtained that $CR = 0.042 < 0.1$, satisfying the consistency test. From Equation (23), the weights of each factor in the Factor Layer on the comprehensive evaluation indicator are 0.061, 0.506, 0.088, and 0.345, respectively. It can be seen that the greatest degree of comprehensive influence on crushing performance is the normal velocity component at the outlet of the propeller, and the smallest is the rotational speed.

4.5. Comprehensive Prediction Results and Analysis of Crushing Performance

U is the set of comprehensive evaluation indicators of crushing performance, and $P = (\overline{P_1}, \overline{P_2}, \overline{P_3}, \overline{P_4})$ = (the maximum wear height of the bushing, the mass flow rate of the particles at the outlet, the average accumulation speed of the particles in the crushing unit, the specific power). $\omega = (a_1, a_2, a_3, a_4)$, a_1, a_2, a_3 and a_4 are the weights of the maximum wear height of the bushing, the mass flow rate of the particles at the outlet, the

average accumulation speed of the particles in the crushing unit, and the specific power, respectively. Because the units of $\overline{P_1}$, P_2, $\overline{P_3}$, and $\overline{P_4}$ are not consistent, they need to be dimensionless. Since the maximum wear height of the bushing, the average accumulation speed of the particles in the crushing unit, is as small as possible, the mass flow rate of the particles at the outlet, and the specific power is as large as possible, the dimensionless formula is:

$$P_{2j} = (x_{2j} - x_{2\min})/(x_{2\max} - x_{2\min}), \ (j = 1, \ 2, \ \ldots, \ 10) \tag{25}$$

$$\overline{P_{ij}} = (y_{i\max} - y_{ij})/(y_{i\max} - x_{i\min}), \ (i = 1, \ 3, \ 4; \ j = 1, \ 2, \ \ldots, \ 10) \tag{26}$$

where x_{2j} is the actual value of the mass flow rate of particles at the outlet, y_{ij} is the actual value of the maximum wear height of the bushing, the average accumulation speed of the particles in the crushing unit, and the specific power.

The evaluation indicator function is as follows:

$$U_j = a_1\overline{P_{1j}} + a_2P_{2j} + a_3\overline{P_{3j}} + a_4\overline{P_{4j}}, \ (j = 1, \ 2, \ \ldots, \ 10) \tag{27}$$

The resulting dataset U can be used as a crushing performance evaluation indicator set. The weight of the maximum wear height of the bushing a_1 is 0.121, the weight of the mass flow rate of the particles at the outlet a_2 is 0.417, the weight of the average accumulation speed of the particles in the crushing unit a_3 is 0.27 and the weight of the specific power a_4 is 0.192. After dimensionless processing of the four indicators by Equations (25) and (26), the data are substituted into Equation (27) to calculate the comprehensive evaluation indicator set of crushing performance. The result is as follows:

$$U = (0.489, \ 0.464, \ 0.438, \ 0.577, \ 0.576, \ 0.574, \ 0.491, \ 0.468, \ 0.444, \ 0.527, \ 0.567, \ 0.607, \ 0.189, \ 0.410, \ 0.631)$$

According to regression analysis, the prediction model of the comprehensive evaluation indicator of crushing performance is:

$$\begin{aligned} y_U = &-3.8997 + 0.0025x_1 - 2.5356x_2 - 0.0002x_3 + 2.0386x_4 + 0.4844x_2{}^2 \\ &-0.1956x_4{}^2 - 0.0006x_1x_2 - 0.0004x_1x_4 + 0.003x_2x_3 + 0.2563x_2x_4 - 0.0008x_3x_4 \end{aligned} \tag{28}$$

The ANOVA table for the prediction model of the comprehensive evaluation indicator is shown in Table 10.

Table 10. The ANOVA table for the comprehensive prediction model.

Source	SS	df	MS	F	R^2
Regression	4.652	4	1.163	716.519	0.917
Residual	0.016	10	0.002		

Through the calculation of this prediction model, $R^2 = 0.917 > R_{\min}{}^2 = 0.7056$, $F = 716.519 > F_{0.01}(4, \ 10) = 5.99$. The equation-fitting effect meets the requirement.

4.6. Verification of Optimization Results and Comparison before and after Optimization

Solving Equation (28) shows that when the rotational speed, the normal velocity component at the propeller outlet, the mass flow rate at the inlet, and the bushing thickness are 1019.08 r/min, 2.02 m/s, 144.7 g/s, and 4.87 mm, the comprehensive prediction model reaches the maximum value.

4.6.1. Verification of Optimization Results

In order to verify the accuracy of the performance optimization results corresponding to the optimal combination of factors, the results calculated by the prediction models were compared with the CFD-DEM simulation results, and the specific values are shown in Table 11. As can be seen from Table 11, the optimization result of maximum wear height

has an error of 3.87% with the simulation, and the optimization result of export mass has an error of 0.66% with the simulation. The optimization result of mass accumulation speed has an error of 3.37% with the simulation, and the optimization result of specific power has an error of 2.93% with the simulation, which indicates that the optimization results have high accuracy.

Table 11. Comparison of optimization results with CFD-DEM simulation results.

Judgment Matrix	The Maximum Wear Height (mm)	The Mass Flow Rate (g/s)	Accumulation Speed (g/s)	The Specific Power (W/g)
Prediction model	1.61	133.57	11.596	0.365
CFD-DEM Simulation	1.55	132.70	12.00	0.376
Error	3.87%	0.66%	3.37%	2.93%

4.6.2. Comparison and Analysis before and after Optimization

The combination of factors for the above optimal crushing performance is simulated and compared with the indicator values under the original conditions before optimization, and the comparison results are shown in Figure 12.
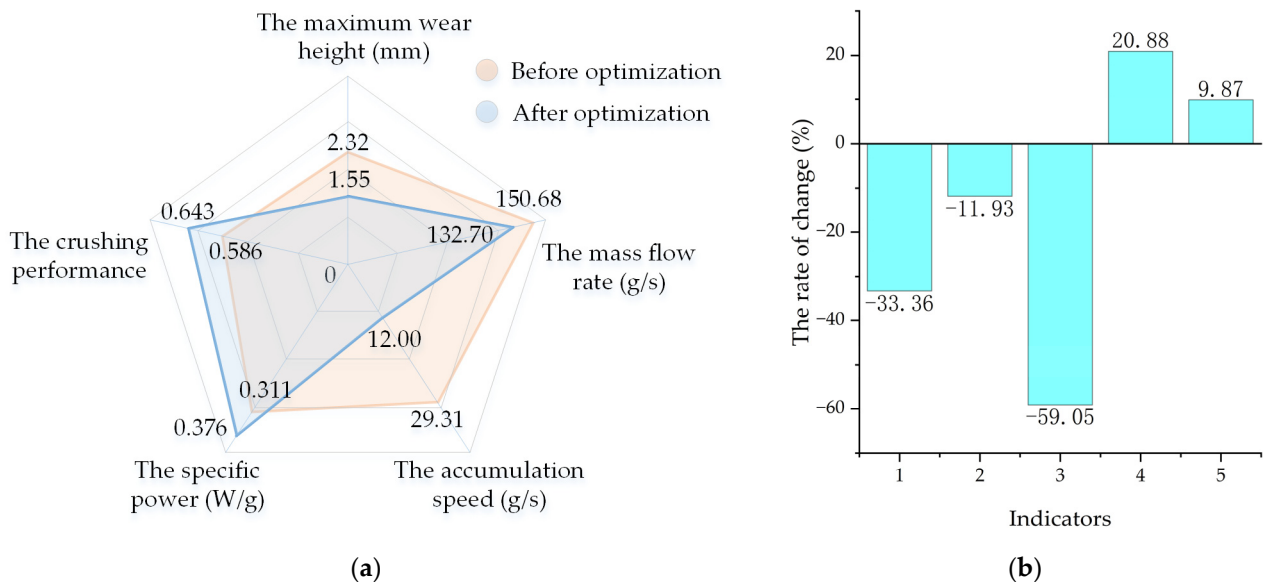

Figure 12. Comparison of results before and after optimization. (**a**) Values of performance indicators before and after optimization; (**b**) Rate of change of each indicator after optimization. In the figure (**b**), 1—The maximum wear height; 2—The mass flow rate; 3—The accumulation speed; 4—The specific power; 5—The crushing performance.

Following optimization, the bushing's maximum wear height is 1.55 mm, and the mass flow rate of particles leaving the crushing unit is 132.70 g/s. The average accumulation speed of particles accumulating in the unit is 12.00 g/s, and the specific power is 0.376 W/g. It can be seen that the maximum wear height of the bushing is reduced by 33.36%, indicating a significant improvement in bushing wear; the mass flow rate of particles at the outlet is reduced by 11.93%, indicating a reduction in the crushing efficiency of the underwater crushing unit. The average accumulation speed of particles in the crushing unit is reduced by 59.05%, indicating a significant increase in the duration of operation of the underwater crushing unit. The specific power increases by 20.88%, indicating that the power consumption of crushing has increased. Each combination of influencing factors in Table 5 was substituted into Equation (28), and the obtained results were compared with the comprehensive evaluation index set U value. Combined with the error analysis, the comprehensive indicator value of the original working condition was 0.586, while the optimal

comprehensive prediction model indicator value was 0.643, so the comprehensive crushing performance was improved by 9.87%. Prior to optimization, the underwater crushing unit had a tendency to achieve better crushing efficiencies, but this led to more severe wear on the bushings and a decrease in the average movement speed of the underwater cleaning robot due to excessive accumulation speed. The AHP balances the underwater crushing unit's performance indicators by reducing bushing wear and accumulation speed at the expense of partial crushing efficiency and power consumption.

5. Conclusions

In this paper, an underwater crushing unit was designed, and a prototype of the underwater crushing unit was fabricated. A CFD-DEM-based simulation model of the underwater crushing unit was established, and grid-independent verification was performed. Validation experiments were designed to measure the quality of barnacle shells discharged from the prototype and to validate the CFD-DEM by comparing it with the simulation results of the CFD-DEM. To obtain the data of evaluation indicators corresponding to various factor combinations, the factor level table developed by the Uniform Design was substituted into CFD-DEM. The prediction model of each indicator was established by performing stepwise regression analysis, and the optimal combination of factors was obtained using the solver. A performance optimization method based on multiple nonlinear regression and AHP is proposed, which combines decision methods and nonlinear regression predictive model methods and applies them to the performance optimization of the mechanism. The hierarchical structure and judgment matrix between factors and indicators were constructed by applying AHP. After the consistency test and weight calculation, the weights of each indicator were 0.121, 0.417, 0.27, and 0.192, respectively. A prediction model of the comprehensive evaluation indicator was established. The solution of the model showed that when the rotational speed was 1019.08 r/min, the normal velocity component at the propeller outlet was 2.02 m/s, the mass flow rate at the inlet was 144.7 g/s, and the bushing thickness was 4.87 mm; the comprehensive crushing performance was improved by 9.87%.

Future studies will focus on the optimization of the structural parameters of the underwater crushing unit in order to improve the performance of the device. New prototypes will be made based on the optimized parameters. Future research will focus on reducing the vibrations generated during the use of an underwater crushing unit, which can affect the attitude toward underwater cleaning robots.

Author Contributions: Conceptualization, L.W., S.J. and L.S.; methodology, S.J. and D.P.; software, S.J., W.F. and D.X.; validation, L.W., S.J., D.P. and W.F.; formal analysis, S.J.; investigation, S.J. and D.P.; resources, S.J. and L.W.; data curation, S.J.; writing—original draft preparation, S.J.; writing—review and editing, S.J.; visualization, D.P. and B.T.; supervision, L.W. and D.X.; project administration, L.W. and L.S.; funding acquisition, L.W. and S.J. All authors have read and agreed to the published version of the manuscript.

Institutional Review Board Statement: Not applicable.

Informed Consent Statement: Not applicable.

Data Availability Statement: Data are contained within the article.

Conflicts of Interest: The authors declare no conflict of interest.

References

1. Farkas, A.; Degiuli, N.; Martic, I.; Dejhalla, R. Impact of Hard Fouling on the Ship Performance of Different Ship Forms. *J. Mar. Sci. Eng.* **2020**, *8*, 748. [CrossRef]
2. Hakim, M.L.; Nugroho, B.; Nurrohman, M.N.; Suastika, I.K.; Utama, I.K.A.P. Investigation of fuel consumption on an operating ship due to biofouling growth and quality of anti-fouling coating. *IOP Conf. Ser. Earth Environ. Sci.* **2019**, *339*, 012037. [CrossRef]
3. Schultz, M.P.; Bendick, J.A.; Holm, E.R.; Hertel, W.M. Economic impact of biofouling on a naval surface ship. *Biofouling* **2011**, *27*, 87–98. [CrossRef] [PubMed]
4. Champ, M.A. A review of organotin regulatory strategies, pending actions, related costs and benefits. *Sci. Total Environ.* **2000**, *258*, 21–71. [CrossRef] [PubMed]
5. Farkas, A.; Degiuli, N.; Martic, I. Assessment of the effect of biofilm on the ship hydrodynamic performance by performance prediction method. *Int. J. Nav. Archit. Ocean. Eng.* **2021**, *13*, 102–114. [CrossRef]
6. Dinariyana, A.A.B.; Deva, P.P.; Ariana, I.M.; Handani, D.W. Development of Model-Driven Decision Support System to Schedule Underwater Hull Cleaning. *Brodogradnja* **2022**, *73*, 21–37. [CrossRef]
7. Degiuli, N.; Farkas, A.; Martic, I.; Grlj, C.G. Optimization of Maintenance Schedule for Containerships Sailing in the Adriatic Sea. *J. Mar. Sci. Eng.* **2023**, *11*, 201. [CrossRef]
8. Narewski, M. Hismar—Underwater Hull Inspection and Cleaning System as a Tool for Ship Propulsion System Performance Increase. *J. Pol. CIMAC* **2009**, *4*, 227–232.
9. Tahir, A.; Iqbal, J. Underwater robotic vehicles: Latest development trends and potential challenges. *Sci. Int.* **2014**, *26*, 1111–1117.
10. Sakagami, N.; Shibata, M.; Hashizume, H.; Hagiwara, Y.; Ishimaru, K.; Ueda, T.; Saitou, T.; Fujita, K.; Kawamura, S.; Inoue, T.; et al. Development of a human-sized ROV with dual-arm. In Proceedings of the Oceans'10 IEEE, Sydney, Australia, 24–27 May 2010; pp. 1–6.
11. Christ, R.D.; Wernli, R. *The ROV Manual: A User Guide for Remotely Operated Vehicles*; Butterworth-Heinemann: Oxford, UK, 2013.
12. Hua, J.; Chiu, Y.-S.; Tsai, C.-Y. En-route operated hydroblasting system for counteracting biofouling on ship hull. *Ocean Eng.* **2018**, *152*, 249–256. [CrossRef]
13. Ralys, A.; Moksin, V. Numerical simulation of a cavitating pulsating water jet used for removing contaminants from metal surfaces. *Trans. FAMENA* **2019**, *43*, 69–80. [CrossRef]
14. Zhong, X.; Dong, J.M.; Liu, M.S.; Meng, R.X.; Li, S.; Pan, X.X. Experimental study on ship fouling cleaning by ultrasonic-enhanced submerged cavitation jet: A preliminary study. *Ocean. Eng.* **2022**, *258*, 111844. [CrossRef]
15. Tian, Z.; Feng, J.H.; Chen, X.; Lei, Z.L.; Chen, Y.B. Hybrid laser cleaning characteristic of marine barnacles fouling attached on Al alloys. *J. Laser Appl.* **2021**, *33*, 042036. [CrossRef]
16. Fan, J.; Yang, C.; Chen, Y.; Wang, H.; Huang, Z.; Shou, Z.; Jiang, P.; Wei, Q. An underwater robot with self-adaption mechanism for cleaning steel pipes with variable diameters. *Ind. Robot: Int. J.* **2018**, *45*, 193–205. [CrossRef]
17. Wang, B.; Ni, Z.; Shen, Y.; Zhang, S.; Shen, Q.; Niu, X.w. Design and analysis of a wheel-leg compound variable curvature ship hull cleaning robot. *Ocean Eng.* **2022**, *266*, 112755. [CrossRef]
18. Chen, L.; Cui, R.; Yan, W.; Xu, H.; Zhao, H.; Li, H. Design and climbing control of an underwater robot for ship hull cleaning. *Ocean Eng.* **2023**, *274*, 114024. [CrossRef]
19. Hachicha, S.; Zaoui, C.; Dallagi, H.; Nejim, S.; Maalej, A. Innovative design of an underwater cleaning robot with a two arm manipulator for hull cleaning. *Ocean Eng.* **2019**, *181*, 303–313. [CrossRef]
20. Park, D.; Han, J.-B.; Yeu, T.; Cho, S.-g.; Kim, S.; Kim, H.; Lee, Y. Development of an Autonomous Cleaning Robot with a Hydraulic Manipulator Arm for the Cleaning of Niche Areas of a Ship Hull. *J. Mar. Sci. Eng.* **2023**, *11*, 973. [CrossRef]
21. Vu, M.T.; Choi, H.S.; Ji, D.H.; Jeong, S.K.; Kim, J.Y. A study on an up-milling rock crushing tool operation of an underwater tracked vehicle. *Proc. Inst. Mech. Eng. Part M J. Eng. Marit. Environ.* **2019**, *233*, 283–300. [CrossRef]
22. Ramesh, N.R.; Thirumurugan, K.; Raphael, D.C.; Ramadass, G.A.; Atmanand, M.A. Development and Subsea Testing of Polymetallic Nodule Crusher for Underwater Mining Machine. *Mar. Technol. Soc. J.* **2021**, *55*, 65–72. [CrossRef]
23. Ferziger, J.H.; PeriC, M. *Computational Methods for Fluid Dynamics*; Springer: Berlin/Heidelberg, Germany, 2012.
24. Khalifa, G.M.; Weiner, S.; Addadi, L. Mineral and Matrix Components of the Operculum and Shell of the Barnacle Balanus amphitrite: Calcite Crystal Growth in a Hydrogel. *Cryst. Growth Des.* **2011**, *11*, 5122–5130. [CrossRef]
25. Vinagre, P.A.; Simas, T.; Cruz, E.; Pinori, E.; Svenson, J. Marine Biofouling: A European Database for the Marine Renewable Energy Sector. *J. Mar. Sci. Eng.* **2020**, *8*, 495. [CrossRef]
26. Fang, H.Y.; Xing, D.W.; Yang, J.H.; Liu, F.L.; Chen, J.L.; Li, J.S. Experimental Study on Limestone Cohesive Particle Model and Crushing Simulation. *Adv. Mater. Sci. Eng.* **2018**, *2018*, 3645720. [CrossRef]
27. Tavares, L.M. Review and Further Validation of a Practical Single-Particle Breakage Model. *KONA Powder Part. J.* **2022**, *39*, 62–83. [CrossRef]
28. Zheng, G.; Zhu, N.; Tian, Z.; Chen, Y.; Sun, B. Application of a trapezoidal fuzzy AHP method for work safety evaluation and early warning rating of hot and humid environments. *Saf. Sci.* **2012**, *50*, 228–239. [CrossRef]